INSTITUTE OF PHYSICS PUBLISHING PLASMA PHYSICS AND CONTROLLED FUSION

Plasma Phys. Control. Fusion **48** (2006) 1063–1076 doi:10.1088/0741-3335/48/8/002

Fast electron transport and ionization in a target irradiated by a high power laser

A P L Robinson[1,2], **A R Bell**[2] **and R J Kingham**[2]

[1] Central Laser Facility, CCLRC Rutherford-Appleton Laboratory, Chilton, Didcot, Oxfordshire, OX11 0QX, UK
[2] Blackett Laboratory, Imperial College London, SW7 2BZ, UK

Received 1 February 2006, in final form 30 March 2006
Published 5 July 2006
Online at stacks.iop.org/PPCF/48/1063

Abstract

The propagation of relativistic (fast) electrons produced by ultraintense laser irradiation into solid targets is crucial to important fields of laser–plasma study including Fast Ignitor ICF and ion acceleration. In current experiments, targets are initially at room temperature, and there is a need to determine the extent to which the solid–plasma transition affects fast electron transport. A Vlasov–Fokker–Planck code with ionization physics is used to simulate laser–solid interactions around $10^{18}\,\mathrm{W\,cm^{-2}}\,\mu\mathrm{m}^2$. Both field and collisional ionization physics is included, and the target is initially unionized. We find that both field and collisional ionization are important to the initial breakdown. After the initial breakdown, collisional ionization continues to ionize the target, and this affects the electric field structure. The effect of continual ionization is for the cold electron distribution to be non-Maxwellian, and for the ionization state to vary throughout the target. This will be important for 'interior' ion acceleration, magnetic field generation and the transverse structure of the fast electron beam.

1. Introduction

The absorption of energy into relativistic (fast) electrons in ultraintense laser–solid interactions ($I\lambda^2 > 10^{18}\,\mathrm{W\,cm^{-2}}\,\mu\mathrm{m}^2$) has attracted considerable attention. The fast electron energy can be used for heating or ion acceleration; however this may occur hundreds of microns away from the absorption region. The transport of these fast electrons through the solid target is therefore of paramount importance. In particular it is of direct importantance to fast ignition ICF [1, 2], and it is a major issue in proton acceleration studies [3, 4].

Given that, experimentally [5], stark differences have been observed between metallic and insulating targets with regard to fast electron propagation, there is a need to understand fast electron transport in an initially unionized insulating target. Many experiments are done with targets at room temperature, and the fast electrons require charge and current neutralization in order to propagate into the target. In the case of an initially unionized insulator, the material

must first undergo a breakdown into a plasma, in order to provide the return current. The breakdown process and subsequent ionization will significantly affect the electric field structure and thus the fast electron energy losses. Particle-in-cell methods (PIC) with ionization and collision models have been used previously [6,7], but the Vlasov–Fokker–Planck (VFP) codes are better suited to the modelling of low temperature plasmas and the details of ionization, particularly in the presence of a low density high energy fast electron population. Town [8] and Ethier and Matte [9], in particular observed non-Maxwellian cold electron distributions at subrelativistic laser intensities using VFP codes that worked in the diffusive approximation. It is not clear that similar observations have been made using PIC codes, or if such observations should be made when relativistic electrons propagate deep into a target. Strongly non-Maxwellian cold electron distributions will have a significant effect on target conductivity which is crucial to fast electron transport. The works of [6,10], both considered a subrelativistic intensity ($10^{17}\,\mathrm{W\,cm^{-2}}\,\mu\mathrm{m}^2$), and very thin targets (400 nm). In terms of solid density targets, so far only Zhidkov [11] has considered the ultraintense regime ($10^{19}\,\mathrm{W\,cm^{-2}}\,\mu\mathrm{m}^2$) using a collisional (albeit this is done in a sophisticated manner) PIC code with ionization physics; however a 200 nm Al foil was simulated, and not a thick insulating target.

There are certain concerns that arise from using PIC codes to model laser–solid related processes. Firstly, PIC does have the problem of statistical noise. The noise decreases with the number of macroparticles, N, but only as $\propto 1/\sqrt{N}$. Statistical noise can be reduced using more macroparticles in a simulation; however this requires more computational resources. As a means of representing the distribution function in momentum, a macroparticle representation where all the quasiparticles are equivalent has a limited dynamic range that depends on the number of macroparticles per cell. Modern PIC codes have reduced this problem using schemes where particles have different weights. However, in certain situations, such as when a few heavily weighted particles move into a region consisting of lightly weighted particles, this can be deleterious to the simulation statistics. There are other issues involved with the PIC method such as numerical instabilities in momentum-conserving codes that lead to heating or cooling, which may be problematic. These problems have been reduced by using more advanced algorithms for projecting macroparticle charge onto the grid, and more so by the recent introduction of energy-conserving methods in PIC [12]. Energy conserving PIC [13,14] and hybrid-PIC methods [15, 16] have allowed considerably lower starting temperatures (on the order of 100 eV) to be used in simulations. In contrast, a continuum representation of the distribution function, solved by finite-difference methods, is virtually noiseless, has high dynamic range, and is not subject to any heating instability. To perform calculations based on an Eulerian gridding of phase space, even with only one or two spatial dimensions, leads to excessive memory requirements. We have overcome these limitations by employing a code based on a spherical harmonic decomposition of the distribution function. This allows us to adopt a finite-difference approach with reduced memory requirements. Such methods may provide a good complement to PIC codes when studying fast electron transport.

In this paper the results of 1D VFP simulations of fast electron propagation into an initially cold, unionized, insulating solid are presented. The target is 60 μm of carbon. The parameters used are relevant to ultraintense laser–solid interactions around $10^{18}\,\mathrm{W\,cm^{-2}}\,\mu\mathrm{m}^2$. The code we use is a 1D version of KALOS, a unique VFP code [17] that includes collisional and field ionization (FI). We relate our results to experimental observations.

There is a body of evidence [5, 18, 19] that indicates that when fast electrons propagate through insulating materials the beam becomes highly filamented. It is not yet clear exactly what causes this. Krasheninnikov [20] has proposed an essentially electrostatic mechanism for the disruption of the ionization front; however this requires further investigation. Additionally there is also experimental evidence of fast electron inhibition due to electric fields [21], although

the range of the fast electrons in a given material depends on the laser intensity. In the case of insulators this is not fully understood. Inhibition due to electric fields also occurs in targets containing an insulating foam layer [10]. In this paper we first report the results of a short (200 fs) run and we discuss how ionization dynamics affects fast electron propagation. We also report on other simulations and comparisons with experimental results.

2. Theory

Equation (1) is regarded as being central to fast electron transport in solid targets [22]. This must hold to a good approximation, or electric fields large enough to stop the fast electrons would quickly be generated.

$$\boldsymbol{j}_{\text{fast}} + \boldsymbol{j}_{\text{return}} = \boldsymbol{0}. \tag{1}$$

In a conducting solid or plasma, the electric field will be determined by the relation.

$$\boldsymbol{E} = \eta \boldsymbol{j}_{\text{return}} = -\eta \boldsymbol{j}_{\text{fast}}. \tag{2}$$

In the case where fast electrons propagate into a region of vacuum, or an unionized insulator, equations (1) and (2) will no longer apply, and sheath formation must occur. It is expected that a strong electric field will build up, and that this will drive the ionization of the material. A static analytical solution of the plasma–vacuum sheath [23] has shown that the relevant scale length is the fast-electron Debye length, $\lambda_{\text{D,f}} = \sqrt{\varepsilon_0 k_{\text{B}} T_{\text{f}} / n_{\text{f}} e^2}$, and that the peak electric field is approximately, $E \approx \sqrt{2 n_{\text{f}} k_{\text{B}} T_{\text{f}} / \varepsilon_0}$, where n_{f} is the fast electron density, and T_{f} is the fast electron temperature [23]. In the case of propagation into an insulator, the breakdown of the target will produce cold electrons which will reduce the charge separation, so a larger scale-length and smaller electric field are expected. Indeed this was shown by Tikhonchuk [24], in his 1D model, in which he considered the FI of an insulator, and a step-like fast electron front. Some time after this breakdown, once a sufficient number of cold electrons has been liberated, current balance (equation (1)) should apply. Once breakdown has occurred, the electric field present will be determined by the plasma resistivity caused by cold electron collisions. In contrast, the fast electron (K.E. >100 keV) collision time is of the order of 1 ps at solid density, so the fast electron dynamics are dominated by the electromagnetic fields.

The two important ionization processes are FI and collisional ionization (CI) [24, 11]. In FI, the presence of the electric field alone liberates electrons by distorting the potential that bound electrons experience. In the low field limit, this distortion permits quantum mechanical tunnelling of electrons from bound states to free states. For a hydrogenic atom the FI rate (W_{fi})is given by equation (3), in which the atomic frequency is $\omega_{\text{at}} = 4.13 \times 10^{16}\,\text{s}^{-1}$, the ionization energy of hydrogen is $U_{\text{H}} = 13.6$ eV, the ionization energy of the atom/ion is U_{Z}, the atomic field is $E_{\text{at}} = 5.14 \times 10^{11}\,\text{V m}^{-1}$, and the electric field is E [25]. This is valid in the regime where $E \ll E_{\text{at}}$.

$$W_{\text{fi}} = 4\omega_{\text{at}} \left(\frac{U_{\text{Z}}}{U_{\text{H}}}\right)^{5/2} \frac{E_{\text{at}}}{E} \exp\left(-\frac{2E_{\text{at}}}{3E}\left(\frac{U_{\text{Z}}}{U_{\text{H}}}\right)^{3/2}\right). \tag{3}$$

Numerical solutions of the time-dependent Schrödinger equation have shown that equation (3) is a good approximation up to $E = E_{\text{crit}}$ which is given by equation (4) [26]. In the high field limit ($E > E_{\text{crit}}$), the atomic field is negligible and the electron becomes instantaneously unbound. This is referred to as barrier-suppression ionization (BSI). Although the E_{crit} case is included in our computational model, the electric field does not reach E_{crit} in our simulation.

$$E_{\text{crit}} = E_{\text{at}}(\sqrt{2} - 1)\left(\frac{U_{\text{Z}}}{2U_{\text{H}}}\right)^{3/2}. \tag{4}$$

In CI, bound electrons are liberated by collisions with sufficiently energetic, unbound electrons. The cross-section for electron impact ionization can be taken from the Lotz formula [27], which is a fit to empirical data.

$$\sigma \approx 4 \times 10^{-18} \xi \frac{\log(\epsilon / U_Z)}{\epsilon U_Z} \, \mathrm{m}^{-2} \tag{5}$$

ξ is the number of equivalent electrons in the ion shell, ϵ is the incident electron energy in electronvolts, and U_Z is the ionization energy in electronvolts. The Lotz formula gives a total cross-section, i.e. integrated over all angles. If the angular dependence is neglected, the rate of CI (W_c) then becomes the integration over the electron distribution function given in equation (6).

$$W_c = \int_0^\infty 4\pi p^2 \sigma(p) v(p) g(p) \, \mathrm{d}p. \tag{6}$$

In equation (6), p is the magnitude of momentum, v is magnitude of velocity and $g(p)$ is the isotropic component of the distribution function (i.e. zeroth order component in a spherical harmonic decomposition). Since the Lotz cross-section peaks at $\varepsilon = U_z$e (e is the base of the natural logarithm), for the first few ionizations (which are of the order of tens of electronvolts) the cold electron contribution to W_c may be significant. The analysis of breakdown due to FI alone done by Tikhonchuck [24] showed that for short pulse laser–plasma parameters the electric field behind the fast electron front is about $10\,\mathrm{GV\,m^{-1}}$ and that the width of the breakdown region is of the order of a micrometre. At $E = 10\,\mathrm{GV\,m^{-1}}$, the rate of FI is much greater than the estimated rate of CI due to fast electrons, so it is reasonable that CI due to fast electrons is neglected in this calculation. In [24] it is found that the first ionization of the target material is not completed. Since the electrostatic potential across the breakdown region is of the order of 10 kV, it is possible that the cold electrons might be accelerated to energies exceeding the first few ionization energies, and thereby cause further ionization. Therefore, one might expect that CI by cold electron might complete the first ionization, and perhaps ionize the target to higher charge states. As the self-consistent calculation of the entire electron distribution including ionization by cold electrons is required, a detailed kinetic simulation has been carried out.

The full computational model requires a source of fast electrons. A fully realistic description of the fast electrons entering the target would require the process of laser absorption to be simulated. This is beyond the scope of this paper, and instead we treat absorption only as an energy deposition. Experimental measurements of the fast electrons emerging from the back of the target have found that the energy spectrum approximates to a Maxwellian characterized by a fast electron temperature, so in the computational model we inject fast electrons with a Maxwellian distribution. For $I\lambda^2 < 10^{19}\,\mathrm{W\,cm^{-2}}\,\mu\mathrm{m}^2$, $T_f = (2.5 \times 10^{-4})(I\lambda^2(\mathrm{W\,cm^{-2}}\,\mu\mathrm{m}^2))^{1/3}$ keV provides a good fit to experimental data [28].

3. Computational model

The simulation results presented are the results of calculations carried out using KALOS, a unique finite-difference VFP code, a description of which is given in [17, 29]. In one spatial dimension KALOS uses a Legendre polynomial decomposition of the distribution function. The Vlasov component of the code is fully relativistic. Both electron–ion and electron–electron collisions are included, but with non-relativistic collision operators. This is acceptable, because the collision time for the fast electrons considerably exceeds the simulation time. The electron distribution function only is solved for, with the ions remaining stationary. Laser physics is not included, with fast electrons being generated artificially in a 'heating region'. This method

was previously used in [17]. In this region, in each time-step and spatial cell, a fraction of electrons from all momentum cells are removed, and replaced by an equal total number of electrons with the distribution given by equation (7).

$$f_{\text{fast}} \propto \exp\left(\frac{-\sqrt{p^2c^2 + m_e^2c^4}}{T_f}\right). \tag{7}$$

This distribution is isotropic, i.e. decomposes into f_0 only. The fraction of electrons that are removed at each time step is determined from a prescribed heating power. The heating power per unit volume, P, has a spatial and temporal dependence given by equation (8). The fraction of electrons that are heated is then given by $P\Delta t/\langle U_{\text{fast}}\rangle n_e$, where $\langle U_{\text{fast}}\rangle$ is the average fast electron energy from equation (7).

$$P = P_0 \cos^2\left(\frac{\pi x}{2x_h}\right)\sin\left(\frac{\pi t}{\tau_h}\right). \tag{8}$$

Fast electrons are generated for $0 < t < \tau_h$. No heating is done for $t > \tau_h$. The spatial extent of the heating region is x_h, and no heating is done for $x > x_h$. The version of KALOS used has only one spatial dimension, and thus has only one component of the electric field, and no magnetic field. The spatial advection routines uses reflective boundary conditions. In this code the distribution function is always axisymmetric about the p_x axis. Reflective boundaries are appropriate, because this is equivalent to confinement in the target by thin sheath fields at the plasma–vacuum interface.

In a previous publications where KALOS was used [17], the volume of target being simulated was initially fully ionized, and at a temperature of about 300 eV. Recently we have included the FI process, and the electron impact (CI) process via a simple model. The rate of FI in each spatial cell is estimated from the ionization probability formula, equation (3). In the case of CI, in each spatial cell, the number of ionizing collisions due to each momentum cell is estimated to be $4\pi p^2 f_0(p, x)\Delta(p)v(p)\sigma(\epsilon(p))$, where the cross-section, σ, is taken from equation (5).

In the case of FI, the rate equations are solved implicitly, and the 'ionization current' is accounted for, as in [30]. In the case of CI we make the approximation that the liberated electron has minimal energy, as in Town's previous inclusion of CI in a VFP code [8]. The ionizing electron loses energy equal to the ionization energy. If the new $|\boldsymbol{p}|$ lies in the same momentum cell then the energy loss is handled using a modification to the electron–electron collision routine. If the new $|\boldsymbol{p}|$ lies in a lower momentum cell then the energy loss is handled by subtracting electrons from that cell and adding isotropized electrons to the lower cell. Liberated electrons are put into the first five cells of f_0 (assume that liberated electrons are rapidly isotropized) according to the distribution $e^{-p^2/2\beta^2}$, where β is an arbitrary parameter(fixed throughout the simulation). This was done to avoid any numerical problems that might have been caused by putting all the liberated electrons into a single cell, and to allow the liberated electrons to have a finite energy spread. In a previous work by Town *et al* [8] the liberated electrons were all placed in the lowest momentum cell, and in work by Ethier and Matte [9], the liberated electrons were placed in the lowest two momentum cells. One may regard the beta parameter as characterizing the energy spread of the liberated electrons. Physically the liberated electrons will have a finite energy spread, although this depends on detailed atomic physics that can be difficult to include in a plasma code. This feature of the code allowed us to consider the effects of varying the energy spread of the liberated electrons. Each ionization state is tracked as a separate population. In this model there are no excited states, and no recombination.

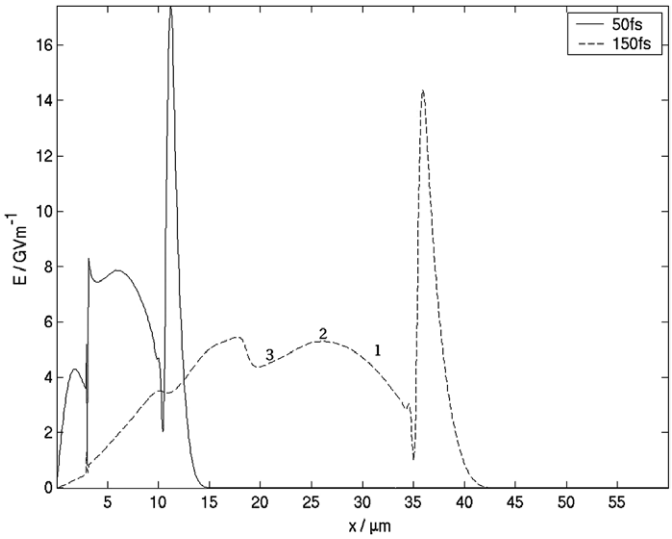

Figure 1. Electric field profiles at 50 and 150 fs.

4. Results and discussion

In our simulation, a uniform spatial grid 60 μm long with $\Delta x = 0.05\,\mu$m is used. The momentum grid consists of two uniform sections of different Δp, with Δp being increased gradually over several grid points between the two sections. Up to $p = 1.5 \times 10^{-23}\,\mathrm{kg\,ms^{-1}}$, the momentum cell size is small, and set at $\Delta p_{\mathrm{cold}} = 10^{-25}\,\mathrm{kg\,ms^{-1}}$, which is sufficient to resolve the ionization energies. Above $p = 1.5 \times 10^{-23}\,\mathrm{kg\,ms^{-1}}$ the momentum cell size is gradually increased to $\Delta p = 2 \times 10^{-24}\,\mathrm{kg\,ms^{-1}}$. The parameter β in the ionization routines is set to $2\Delta p_{\mathrm{cold}}$. The distribution function is expanded up to the $l = 20$ Legendre polynomial. The first 3 μm consists of fully ionized carbon at a density of $1.8\times10^{29}\,\mathrm{m^{-3}}$, with the electron temperature at 50 eV. While this initialization of 0–3 μm does not represent thermodynamic equilibrium, this is done to ensure that the heating region is initially uniform and fully ionized, so that there are no numerical errors incurred in the injection of the fast electrons. From 3 to 60 μm, the target consists of unionized carbon at the same density. The parameters of the heating expression, equation (8) are set at $x_{\mathrm{h}} = 2.5\,\mu$m, and $\tau_{\mathrm{h}} = 100$ fs. The heating power per unit volume is set at $P_0 = 5.65\times10^{27}\,\mathrm{W\,m^{-3}}$, which gives approximately the same power flux as laser irradiation at $10^{18}\,\mathrm{W\,cm^{-2}}$ with a 50% conversion into fast electron energy. The fast electron temperature, T_{f} is set to 300 keV. The simulation time is 200 fs.

The electric field at 50 and 150 fs is shown in figure 1. Throughout the simulation the electric field can be described as consisting of two structures. First, there is a spike that moves into the target and that is close to the fast electron front, and second there is a set of undulations that develop behind the peak. The peak of the electric field that is associated with the fast electron front (which we refer to as the 'front-field') moves into the target with a velocity that starts at about $2.3 \times 10^8\,\mathrm{m\,s^{-1}}$, and which gradually increases to about $2.5 \times 10^8\,\mathrm{m\,s^{-1}}$. The peak electric field in the front is in the range $1 \times 10^{10} < E < 2 \times 10^{10}\,\mathrm{V\,m^{-1}}$ up to 190 fs. The front-field has a full width half maximum (FWHM) of 0.85 μm at 20 fs, which broadens to 1.45 μm at 100 fs, and 1.95 μm at 150 fs. Behind the fast electron front the undulations in the electric field seen at later times are associated with progressive ionization of the target.

We can estimate the effect on the fast electrons by treating the front-field as a travelling 'square pulse' of electric field. Let the electric field in this region be E, its length be L, and the velocity be v (with corresponding Lorentz factor γ_v). In the frame which is co-moving with the field, the electric field is still E, but the length of the front-field is now $\gamma_v L$. The kinetic energy of the electron that almost crosses the field in the co-moving frame is $\gamma_v eEL$, and this must also be the kinetic energy of the maximally slowed electron in the co-moving frame. The 3-momenta of these electrons can be obtained from the mass-energy invariant. The appropriate Lorentz transforms can then be applied to find the kinetic energy of the electrons in the lab frame. The first kinetic energy of interest is that which an electron must have initially to escape through the front-field, κ_{escape} (equation (9)). Electrons with kinetic energy greater than κ_{escape} overtake the front-field. The other kinetic energy of interest is the minimum kinetic energy that an electron can leave the front field with, κ_{slow} (equation (10)). In this case, the electron almost crosses the front-field, but fails to do so, and it is eventually overtaken by the front-field as it decelerates.

$$\kappa_{\text{escape}} = (\gamma_v - 1)m_e c^2 + \gamma_v \left(\gamma_v eEL + \frac{v}{c}\sqrt{\gamma_v^2 e^2 E^2 L^2 + 2\gamma_v eELm_e c^2} \right), \quad (9)$$

$$\kappa_{\text{slow}} = (\gamma_v - 1)m_e c^2 + \gamma_v \left(\gamma_v eEL - \frac{v}{c}\sqrt{\gamma_v^2 e^2 E^2 L^2 + 2\gamma_v eELm_e c^2} \right). \quad (10)$$

If we take the FWHM values of E and L at 50 fs as given by the simulation, i.e. $E = 8\,\text{GV m}^{-1}$, $L = 0.85\,\mu\text{m}$ and $v_f = 2.3 \times 10^8\,\text{m s}^{-1}$, then we find that $\kappa_{\text{escape}} = 430\,\text{keV}$, and $\kappa_{\text{slow}} = 190\,\text{keV}$. The time taken for maximal slowing to occur is approximately 130 fs, so the slowing of the fast electrons takes place on a time-scale that is long compared with the simulation time. This shows that no fast electrons are being stopped (or slowed so much as to become collisional), and that some fast electrons are outrunning the front-field. This is illustrated by figure 3, which is a plot of $p^2 f_0(p, x)$ at 50 fs. $p^2 f_0$ is the integrand of the zeroth moment of the distribution function, which can be thought of as a density plot in $|\boldsymbol{p}| - x$ phase space. The plot shows that the fast electrons are only experiencing a small amount of slowing in the front-field. Fast electrons with velocities exceeding that of the front-field, are moving ahead of the front-field. This velocity dispersion results in the broadening of the peak over time, and the increase in the velocity of the front-field.

The discussion of the fast electron dynamics does open up the interesting question of how our results compare with experimental results. For a 1D code the most appropriate comparison is the fast electron penetration range. Pisani *et al* [21] measured a penetration range in CH of 220 μm at $10^{18}\,\text{W cm}^{-2}$, which was much larger than that of Al (60 μm) at the same intensity. At $10^{19}\,\text{W cm}^{-2}$, the penetration range in CH is 180 μm, and 230 μm in Al. Our simulation is relevant to the lower intensity regime, and since our fast electrons were not strongly inhibited by 200 fs (i.e. a maximum fast electron range of 60 μm) our results agree with these experimental measurements. To be more confident of our results, we carried out a further simulation with a stretched momentum grid and a coarser spatial grid. We also injected the fast electrons for 500 fs, and with a $\cos^4\theta$ distribution. This injects the fast electrons with an approximately 30° half-angle [17], which is more realistic than injecting them isotropically. The run was carried out to 600 fs. In this simulation we found that the fast electron front reached 160 μm, and that the peak of the fast electron density was at 55 μm. This is shown in figure 2. This shows that the fast electrons were able to penetrate the target relatively unimpeded in the first 600 fs, which is what is expected from the experimental result. Given that the electric field at the peak of the fast electron density (where the average fast electron energy is approx. 300 keV) was about $2\,\text{GV m}^{-1}$ (and we only expect the electric field to fall), we can estimate the minimum penetration distance to be $\approx T_f/E + 55\,\mu\text{m}$ which is about 200 μm. The fast

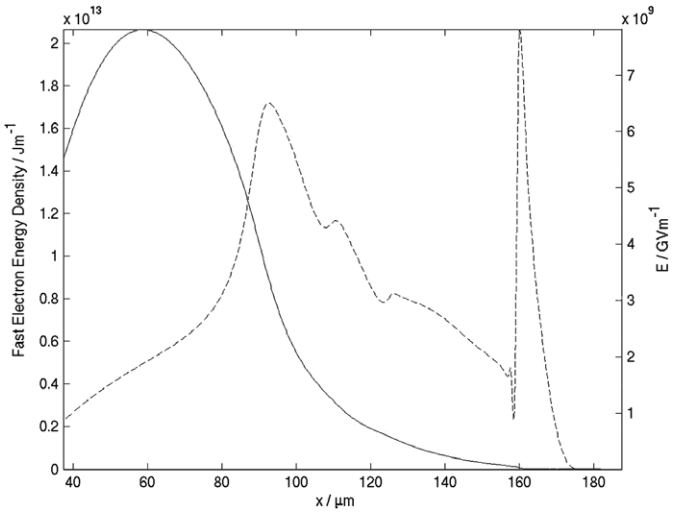

Figure 2. Electric field (- - - -) and fast electron energy density (——) at 600 fs in additional simulation.

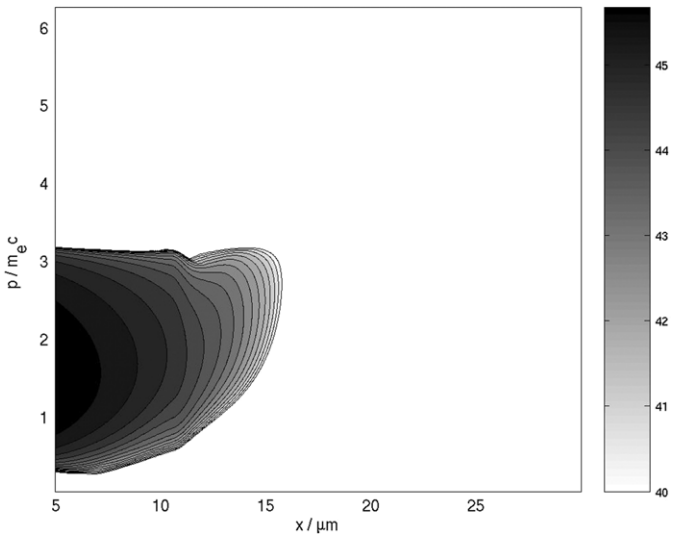

Figure 3. A $\log_{10}(f_0)$ plot at 50 fs. f_0 has units of $\mathrm{kg}^{-3}\,\mathrm{m}^{-6}\,\mathrm{s}^3$. The lower limit on the momentum axis is $0.03 m_e c$. The spatial range is 5–30 μm.

electron temperature at the second largest peak in the electric field at 92.5 μm is also about 300 keV, but there the electric field is 6.5 GV m^{-1}. Fast electrons travelling in this region will be stopped over a distance of $T_f/E \approx 40\,\mu$m so electric field inhibition is important for these electrons. Thus far the code yields very sensible results; however a higher dimensionality and a better atomic physics model is required before proper comparisons to experiments can be made.

In the early stage of propagation into the target, the breakdown at the fast electron front is driven both by CI due to cold electrons, and FI. In figure 4(*a*) we show the FI and CI rates

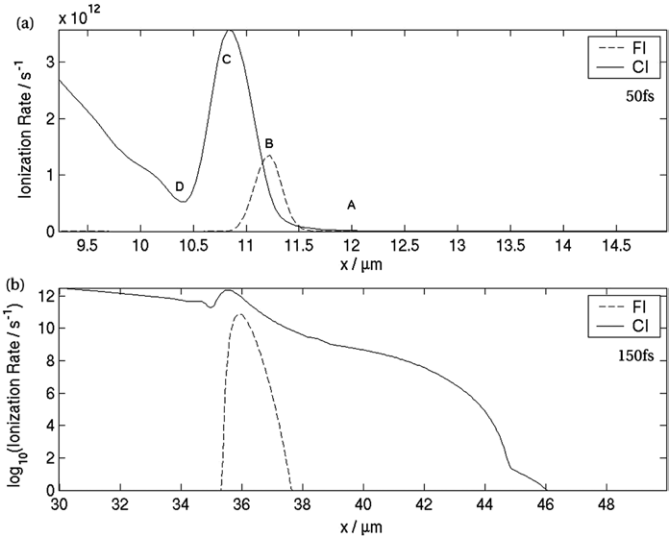

Figure 4. FI and CI rates across the front-field at (*a*) 50 fs, and at (*b*) 150 fs. Note that the lower plot is the $\log_{10}$ plot.

for the first ionization across the fast electron front at 50 fs. The rate of CI is almost entirely due to cold electrons. Points A–D on figure 4(*a*) indicate particular stages in the breakdown at 50 fs. At point A, the front-field is rising but only CI due to fast electrons is occurring. The cold electrons that are being liberated have not yet been accelerated above the first ionization energy, and the electric field is too low for FI. Between points A and B there is a rapid increase in the electric field, and as FI is such a strong function of the electric field, the rate of FI suddenly exceeds the rate of CI. Point B corresponds to the peak of the front field, and we note that at this point the rate of FI is about a factor of two greater than the rate of CI. From B–C the cold electrons have been sufficiently accelerated to cause a rate of CI that exceeds the rate of FI. Eventually enough cold electrons are liberated, and enough acceleration has occurred such that the return current exceeds the fast electron current. As the front-field falls, between points B and C, the rate of FI drops sharply due to the exponential dependence on the electric field. At point C, the rate of CI peaks, as cold electrons have been accelerated between points B and C despite the reduction of the electric field. At point D the CI rate reaches a minimum, because the electric field has been greatly reduced, and energy losses due to ionizing collisions have reduced the number of cold electrons with energy greater than the first ionization energy.

Figure 5(*a*), which shows $\mathrm{d}n/\mathrm{d}\epsilon$ (only 0–80 eV is shown) at four positions at 50 fs, illustrates the breakdown process described above. The four positions are the points A–D on figure 4. The evolution of f_0 from A–C shows the effect of the liberation of cold electrons and the acceleration in the electric field. From A–C the number of cold electrons grows, and the number in the ionizing tail of the distribution grows as well. The value of electron momentum that corresponds to the first ionization energy is indicated by the vertical solid line. Point D shows that, once the electric field is reduced, the number of electrons in the ionizing tail is rapidly reduced.

At 50 fs, FI is clearly important in the breakdown. This is further illustrated by comparison with a simulation where FI was turned off. The electric field profiles at 50 fs are shown in figure 6(*a*). The profiles are similar, but the peak electric field is higher in the simulation without FI. Although the peak electric field is only 30% higher in the simulation without FI, the peak

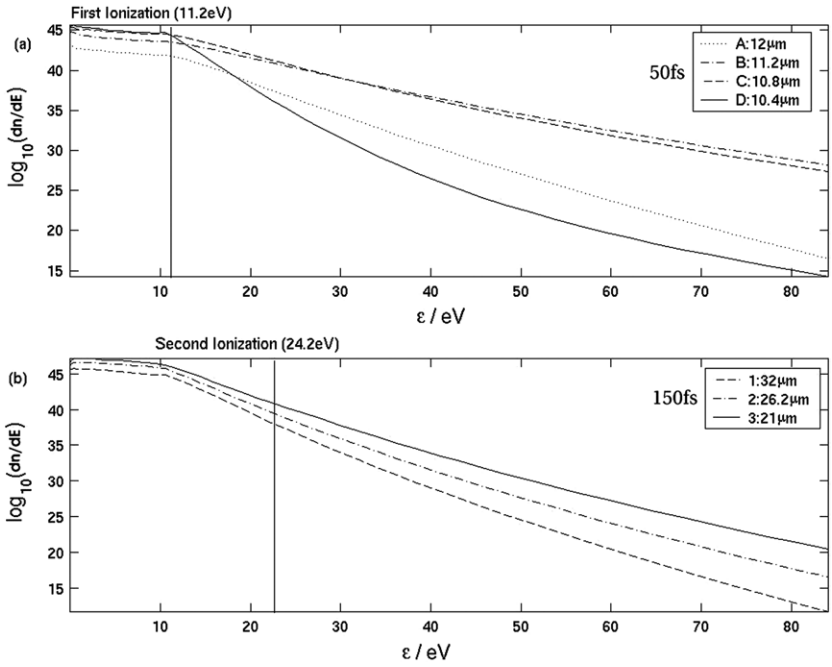

Figure 5. Plots of $\log_{10}(\mathrm{d}n/\mathrm{d}\epsilon)$ at 50 fs (*a*) and at 150 fs (*b*). 50 fs: plots at four positions as indicated in the legend. Points relate to figure 4. 150 fs: plots are at three positions as indicated in the legend. Points relate to figure 1. In both the kinetic energy axis only extends to 84 eV.

electric field in that simulation (24 GV m^{-1}) would cause a FI rate of 5.8×10^{13} s^{-1} (from equation (3)). In the simulation with FI, the maximum FI rate is only 1.35×10^{12} s^{-1}. This shows that, although the two simulations are not greatly different, the result of not including FI is physically unrealistic. Since CI is crucial to the breakdown in this case, the results indicate that both FI and CI are important in the breakdown process.

It is important to examine our method of placing liberated electrons onto the grid. It is particularly important since we have observed non-Maxwellian distributions that check the extent to which our method of placing the liberated electrons on the grid affects the distribution function at low momenta. When β is changed to $4\Delta p_{\mathrm{cold}}$ the electric field profiles are very similar (the largest difference in the electric field profiles is about 7%). Interestingly, this is also true when all the liberated electrons are placed in the lowest momentum cell ($\beta = 0$ case). Other simulations were done with the liberated electrons being placed up to 5 eV and 10 eV, and with β being set at 1.6 eV and 3.3 eV, respectively. The results did not differ significantly from the previous simulations. The effect of Δp was examined next, and a simulation was run which was identical to the standard run except that $\Delta p_{\mathrm{cold}} = 2.5 \times 10^{-25}$ kg ms^{-1} (i.e. cold momentum resolution is decreased by a factor of 2.5). The electric field profile at 50fs is shown in figure 6(*b*), and the electric field profile from the standard run is shown for comparison. The front-fields are almost identical (peak value differs by less than 1%), but behind the front-field the two profiles are different. In fact, the second ionization of the target has occurred faster in the simulation with lower momentum resolution. This is because the difference in kinetic energy between grid points at low momenta is $\Delta\kappa = p\Delta p/m_{\mathrm{e}}$, so resolution of successive ionization thresholds gets worse with p. These tests indicate that our method of placing liberated electrons onto the grid is appropriate, and that the momentum resolution is adequate

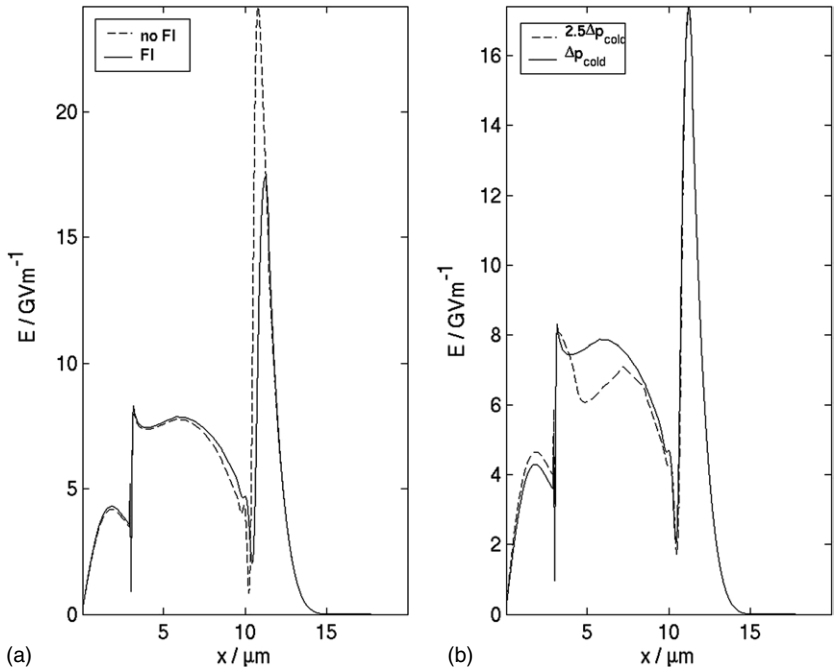

Figure 6. (*a*) Comparison at 50 fs, of two simulations, one with FI and one without FI. (*b*) Comparison at 50 fs, of a standard ($\Delta p_{\rm cold}$) and reduced momentum resolution ($2.5\Delta p_{\rm cold}$) simulation (see text). In both the electric field at 50fs of each simulation is shown in the region 0–20 μm.

as regards the initial breakdown, but they also indicate that momentum resolution is important for capturing the progressive ionization of the target.

At 150 fs, the breakdown process is essentially the same as that described above, except that now FI is unimportant. This is shown in figure 4(*b*) where the FI, and CI rates for the first ionization across the fast electron front are plotted. As was the case at 50 fs, the rate of CI is almost entirely due to cold electrons. The features of additional interest at 150 fs are undulations in the electric field, shown in figure 1, behind the front-field. These undulations are associated with the transitions between ionization states caused by continual CI (by colds) of the target. The number densities of the ions in states $Z = 0$–3 are shown in figure 7 (at 150 fs). A comparison of figures 7 and 1 shows the association of the undulations with the transitions in the ionization state.

The initial rise of the electric field during an undulation is caused by a rise in the fast electron current. This accelerates and heats the cold electrons, increasing the number of cold electrons exceeding the ionization energy threshold for the next ionization state. As more cold electrons are liberated through CI, and then accelerated by the electric field, there is a point (the crest of the undulation) where the return current exceeds the fast electron current. The electric field then decreases. In figure 5(*b*) we plot $\mathrm{d}n/\mathrm{d}\epsilon$ at points 1–3, these are the points that are labelled in figure 1. From points 1–3, it is seen that heating increases the number in the ionizing tail (the threshold for 2nd ionization is shown by the vertical solid line). The gradual decrease in the electric field (points 2–3), unlike the sharp drop in the front-field (cf the earlier description of the front-field), does not result in a drastic reduction of the ionizing tail in the cold distribution. This is expected as from points 1–3 the departure of the electric

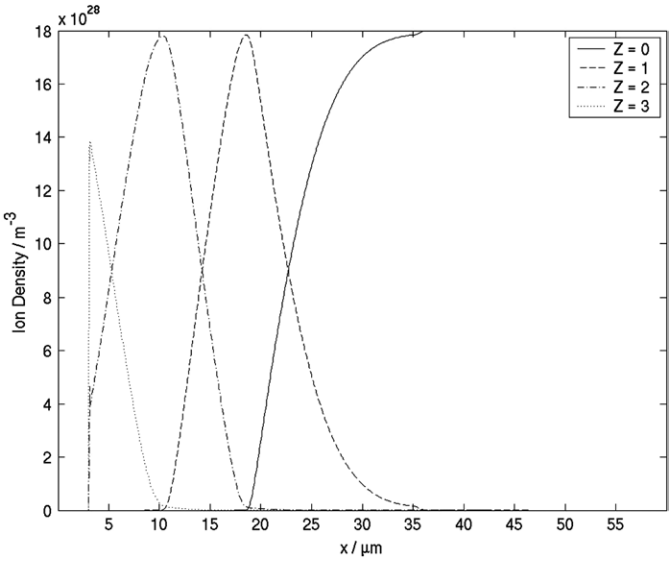

Figure 7. Ion densities for the $Z = 0$–3 states at 150 fs.

field from the average field is only 10% of the average electric field, so we expect continuous, steady heating of the cold electrons.

Throughout the simulation the cold electron distribution is non-Maxwellian. This is caused by the continual ionization, which behind the front field is due to CI. CI distorts the distribution function away from a Maxwellian in two ways. First it adds liberated electrons at very low energies. Second, those electrons with energy greater than the ionization energy (of nearby ions) lose energy through ionizing collisions. This means that most of the electrons must have an energy less than the 'local' ionization energy, and above this 'local' ionization energy the distribution must tail off. These points are illustrated in figure 5, where one sees a high temperature distribution at low energies, then a 'knee' and a low temperature tail at high energies. The tail is due to the ionization loss process, and the high temperature at low energies is due to the liberation process. In contrast, the $\mathrm{d}n/\mathrm{d}\epsilon$ of a Maxwellian distribution is $\propto\sqrt{\epsilon}\mathrm{e}^{-\epsilon/k_\mathrm{B}T}$. Therefore it is clear, on inspecting figure 5, that at low energies the distribution has been 'filled' in, and that the 'knee' at higher energies is also non-Maxwellian.

It is important to assess one weakness of the current model. This is the lack of three-body recombination. Without this the model cannot achieve thermodynamic equilibrium. For the purposes of studying fast electron transport on the sub-picosecond timescale this may not be too important. This however, does not mean that it is unimportant for determining the cold electron distribution. In the work of Kemp *et al* [10], it is argued, by using a simple expression for the three-body recombination rate, that at 1 keV the three-body recombination process is unimportant. This may well be a good approximation at a few hundred electronvolts, but in these simulations the average cold electron energies are below 100 eV. On the other hand, the distribution is strongly non-Maxwellian, and the time-scale of the simulation is very short. Three-body recombination is unlikely to affect the details of the fast electron front in itself, but it may affect what happens far behind the fast electron front. This and other factors make it difficult to assess the extent to which the lack of three-body recombination affects these results. We plan to extend our model to include three-body recombination, and the consequences of this will be reported in future publications.

There has been some suggestion [31,32] that the energetic (multi-megaelectronvolts) ions observed in laser–solid experiments are due to acceleration in the interior of the solid target. The electric field observed in this simulation is not sufficient to produce any significant ion acceleration. The ions only experience a field greater than $10\,\mathrm{GV\,m^{-1}}$ for about 5 fs, after which they experience an average electric field of about 3–5 $\mathrm{GV\,m^{-1}}$. If a proton were to experience a field of $5\,\mathrm{GV\,m^{-1}}$ for 1ps then it would achieve an energy of 1.19 keV. Therefore, our simulation suggests that for the parameters considered, the electric field inside the target should not accelerate ions to megaelectronvolt energies.

5. Summary

We have simulated fast electron propagation into an unionized insulator using a VFP code which includes an ionization model. We observe a thin region of a high electric field that drives the breakdown, and a strong and structured electric field in the post-breakdown region. According to experimental measurements of the fast electron penetration range, strong inhibition of the fast electrons should not be significant in the first 600 fs, and our simulation results agree with this. We have found CI to be crucial everywhere, including (for the parameters considered) the initial breakdown of the target. We have also shown that not including FI leads to unrealistic results. Throughout the simulation, continuing CI leads to a non-Maxwellian cold electron distribution function. The variable ionization state and non-Maxwellian cold distribution function significantly change the plasma resistivity and this is observed in the electric field profile.

The electric field structures observed in this simulation differ significantly from those observed in simulations with a homogeneous fully ionized plasma [17]. On the basis of our results, we suggest that this will have important consequences for magnetic field generation. The stronger electric fields (via $\nabla \times \boldsymbol{E} = -\partial \boldsymbol{B}/\partial t$) are likely to change the global magnetic field structure, and hence the global transverse structure of the beam. It would be interesting to see how this would interact with any electrostatic instabilities [20] of the fast electron front in 2D and 3D, and this current work is an important step towards investigating such physics. A 2D or 3D version of the code used in this paper, along with the improvement of the atomic physics model to include three-body recombination, would be a powerful tool for interpreting experiments. This includes both fast ignition experiments, in which the penetration of fast electrons into CH targets has been studied, and ion acceleration experiments where filamentation may affect the emission of protons from the rear surface of the target.

Acknowledgments

This work was partly supported by the UK Engineering and Physical Sciences Research Council, Grant No GR/R71979/01.

References

[1] Kodama R *et al* 2002 *Nature* **418** 933
[2] Ren C *et al* 2004 *Phys. Rev.* **93** 185004
[3] Snavely R A *et al* 2000 *Phys. Rev. Lett.* **85** 2945
[4] Clark E L *et al* 2000 *Phys. Rev. Lett.* **84** 670
[5] Fuchs J *et al* 2003 *Phys. Rev.* **91** 255002-1–255002-4
[6] Kemp A J *et al* 2004 *Phys. Plasmas* **11** L69–72
[7] Fukuda Y *et al* 2006 *Phys. Rev.* A **73** 031201(R)
[8] Town R P J, Bell A R and Rose S J 1995 *Phys. Rev. Lett.* **74** 924–7

[9] Ethier S and Matte J P 2001 *Phys. Plasmas* **8** 1650
[10] Kemp A J, Pfund R E W and Meyer ter Vehn J 2004 *Phys. Plasmas* **11** 5648
[11] Zhidkov A and Sasaki A 2000 *Phys. Plasmas* **7** 1341–4
[12] Birdsall C and Langdon A 1991 *Plasma Physics via Computer Simulation* (Beograd: Institute of Physics)
[13] Pukhov A 1999 *J. Plasma Phys.* **61** 425–33
[14] Kemp A *et al* 2005 *Phys. Plasmas* **12** 033105
[15] Campbell R 2003 *Phys. Plasmas* **10** 4169
[16] Mason R 2005 *Phys. Rev.* E **72** 015401
[17] Bell A R and Kingham R J 2003 *Phys. Rev. Lett.* **91** 035003
[18] Gremillet L *et al* 1999 *Phys. Rev. Lett.* **83** 5015
[19] Manclossi M *et al* 2006 *Phys. Rev. Lett.* **96** 125002
[20] Krasheninnikov S I *et al* 2005 *Phys. Plasmas* **12** 073105
[21] Pisani F *et al* 2000 *Phys. Rev.* E **62** R5927
[22] Bell A R *et al* 1997 *Plasma Phys. Control. Fusion* **39** 653–9
[23] Passoni M *et al* 2004 *Phys. Rev.* E **69** 026411
[24] Tikhonchuk V 2002 *Phys. Plasmas* **9** 1416–21
[25] Landau L and Liftshitz E 1964 *Quantum Mechanics* (Oxford: Pergamon)
[26] Bauer D and Mulser P 1999 *Phys. Rev.* A **59** 569
[27] Märk T D and Dunn G H 1985 *Electron Impact Ionization* (Berlin: Springer)
[28] Beg F N *et al* 1997 *Phys. Plasmas* **4** 447–57
[29] Bell A R *et al* 2006 *Plasma Phys. Control. Fusion* **48** R37
[30] Mulser P, Cornolti F and Bauer D 1998 *Phys. Plasmas* **5** 4466–75
[31] Davies J R 2002 *Lasers Part. Beams* **20** 243–53
[32] Zepf M *et al* 2001 *Phys. Plasmas* **8** 2323–30